NASA/TM-20205003560

Influence of Particle Velocity and Impingement Angle on Elevated Temperature Solid Particle Erosion of SiC/SiC Ceramic Matrix Composite

Michael J. Presby
Glenn Research Center, Cleveland, Ohio

July 2020

NASA STI Program . . . in Profile

Since its founding, NASA has been dedicated to the advancement of aeronautics and space science. The NASA Scientific and Technical Information (STI) Program plays a key part in helping NASA maintain this important role.

The NASA STI Program operates under the auspices of the Agency Chief Information Officer. It collects, organizes, provides for archiving, and disseminates NASA's STI. The NASA STI Program provides access to the NASA Technical Report Server—Registered (NTRS Reg) and NASA Technical Report Server—Public (NTRS) thus providing one of the largest collections of aeronautical and space science STI in the world. Results are published in both non-NASA channels and by NASA in the NASA STI Report Series, which includes the following report types:

- TECHNICAL PUBLICATION. Reports of completed research or a major significant phase of research that present the results of NASA programs and include extensive data or theoretical analysis. Includes compilations of significant scientific and technical data and information deemed to be of continuing reference value. NASA counter-part of peer-reviewed formal professional papers, but has less stringent limitations on manuscript length and extent of graphic presentations.

- TECHNICAL MEMORANDUM. Scientific and technical findings that are preliminary or of specialized interest, e.g., "quick-release" reports, working papers, and bibliographies that contain minimal annotation. Does not contain extensive analysis.

- CONTRACTOR REPORT. Scientific and technical findings by NASA-sponsored contractors and grantees.

- CONFERENCE PUBLICATION. Collected papers from scientific and technical conferences, symposia, seminars, or other meetings sponsored or co-sponsored by NASA.

- SPECIAL PUBLICATION. Scientific, technical, or historical information from NASA programs, projects, and missions, often concerned with subjects having substantial public interest.

- TECHNICAL TRANSLATION. English-language translations of foreign scientific and technical material pertinent to NASA's mission.

For more information about the NASA STI program, see the following:

- Access the NASA STI program home page at http://www.sti.nasa.gov

- E-mail your question to help@sti.nasa.gov

- Fax your question to the NASA STI Information Desk at 757-864-6500

- Telephone the NASA STI Information Desk at 757-864-9658

- Write to:
  NASA STI Program
  Mail Stop 148
  NASA Langley Research Center
  Hampton, VA 23681-2199

NASA/TM-20205003560

Influence of Particle Velocity and Impingement Angle on Elevated Temperature Solid Particle Erosion of SiC/SiC Ceramic Matrix Composite

Michael J. Presby
Glenn Research Center, Cleveland, Ohio

National Aeronautics and
Space Administration

Glenn Research Center
Cleveland, Ohio 44135

July 2020

Acknowledgments

The author is grateful to Michael Cuy for assistance in the experimental setup of the erosion burner rig facility, Joy Buehler for the preparation of the samples for microscopy, and Bryan Harder for insightful discussions and scientific input.

This report is a formal draft or working paper, intended to solicit comments and ideas from a technical peer group.

This report contains preliminary findings, subject to revision as analysis proceeds.

This work was sponsored by the Transformative Aeronautics Concepts Program.

Level of Review: This material has been technically reviewed by technical management.

Available from

NASA STI Program
Mail Stop 148
NASA Langley Research Center
Hampton, VA 23681-2199

National Technical Information Service
5285 Port Royal Road
Springfield, VA 22161
703-605-6000

This report is available in electronic form at http://www.sti.nasa.gov/ and http://ntrs.nasa.gov/

Influence of Particle Velocity and Impingement Angle on Elevated Temperature Solid Particle Erosion of SiC/SiC Ceramic Matrix Composite

Michael J. Presby
National Aeronautics and Space Administration
Glenn Research Center
Cleveland, Ohio 44135

Summary

Ceramic matrix composites (CMCs) have attracted a lot of attention as an enabling propulsion material system due to their high-temperature properties and have recently been implemented as hot-section components in gas-turbine engines. While significant advancements have been made, challenges still exist for current and next-generation gas turbines; particularly when operating in dust-laden environments. Solid erosive particles can become entrained in the gas flow and impact engine components resulting in significant material removal that can lead to deleterious effects in engine performance. In this study, erosion experiments were conducted on a melt-infiltrated (MI) Silicon carbide fiber-reinforced silicon carbide CMC in a simulated combustion environment at 1,200 °C using 150 μm alumina particles and particle velocities ranging from 100 to 200 m/s. The influence of particle impingement angle was investigated for 30°, 45°, 60°, 75°, and 90°. The CMC was shown to exhibit both a brittle and ductile erosion mode where the contribution of the ductile mode increased as the impingement angle decreased from 90° to 30° as verified by scanning electron microscopy (SEM) of the erosion surface morphologies.

Introduction

Advanced hot-section materials have become a critical technology for current and next-generation gas turbines as the aerospace industry pushes for more powerful and efficient engines. Silicon carbide fiber-reinforced silicon carbide (SiC/SiC) ceramic matrix composites (CMCs) are considered a key enabling propulsion material system for hot-section technology due to their excellent high-temperature capabilities, high strength, toughness, and low density. These characteristics enable improvements in thermal and propulsive efficiency while reducing NO_x emissions (Ref. 1).

While CMCs possess many favorable properties and characteristics, significant design challenges still remain regarding CMCs as hot-section propulsion hardware. This is particularly true for CMC components in gas-turbine engines operating in erosive environments. The damage resulting from the impingement of solid particles can cause significant material removal and strength degradation leading to reduced structural integrity which may ultimately lead to failure. Despite this, there remains little characterization and fundamental understanding of the solid particle erosion processes and mechanisms in CMCs.

Under engine operating conditions, CMCs will be subject to a wide range of erosive conditions (i.e., high-temperature combustion environment, different particle compositions, a range of particle velocities, various impingement angles, etc.). Recently, efforts were undertaken to characterize the erosion response of several gas-turbine-grade CMCs at ambient temperature (Refs. 2 to 4). Results showed that CMCs can be susceptible to significant material removal compared to their monolithic counterparts, and that the damage mechanisms associated with material removal can be complex due to the architectural aspects of the composites. Nonetheless, the erosion response of the CMCs was correlated with macroscopic material

properties such as modulus, bulk density, and apparent matrix hardness. CMCs possessing higher modulus, density, and matrix hardness appeared to have better erosion resistance (Refs. 2 and 3).

A recent investigation (Ref. 3) on the erosion behavior of a melt-infiltrated (MI) SiC/SiC CMC under ambient temperature conditions reported on the effect of particle size at different particle velocities. The findings showed that the particle kinetic energy was a controlling variable in the overall erosion rate of the material. The damage morphology showed that the presence of defects appeared to accelerate the erosion damage, as a localized tunneling effect occurred in regions containing pores, which highlighted the importance of achieving a high-density composite. Additionally, a single impact event showed similar damage features to that observed in monolithic brittle solids, but any predominant cracking systems associated with material removal, such as lateral cracking exhibited in monolithic brittle solids, were not directly identifiable.

In general, and as alluded to in the preceding discussion, the erosion behavior in gas turbines, and in particular CMCs, is governed by numerous factors. As such, continued evaluation of the material response to various erosion conditions is needed. Moreover, it is important to assess the erosion behavior in experimental test rigs that can mimic or replicate conditions similar to those encountered in gas turbines to better understand the operative erosion mechanisms.

The objective of the present work is to systematically investigate the erosion response of an MI SiC/SiC CMC to develop a better understanding of the predominant damage mechanisms associated with material removal over a range of impact velocities and impingement angles. Erosion testing is performed at elevated temperature in a simulated combustion environment to better replicate conditions that engine hardware will experience in service. Scanning electron microscopy (SEM) was utilized posterosion to study the erosion damage and governing mechanisms.

Experimental Procedure

The solid particle erosion experiments in this study were conducted in the NASA Glenn Research Center Erosion Burner Rig Facility. The facility was developed to more accurately represent gas-turbine engine conditions and has been historically used to characterize the solid particle erosion behavior of thermal barrier coatings (TBCs) (Refs. 5 to 7).

Material System

The CMC material system used in this work was a two-dimensional (2D) woven Hi-Nicalon™ Type-S (HNS), boron nitride (BN)-interphase, slurry-cast MI SiC matrix composite. The composite (Panel 1) consisted of eight plies of 5-harness satin-weave fabric oriented in the 0° and 90° directions. The as-received panel thickness was 2.1 mm. Samples were also machined from a second panel (Panel 2) to investigate the consistency in erosion rate from panel to panel. The second panel, manufactured in the same manner, consisted of 12 plies corresponding to an as-received panel thickness of 3.2 mm. Constituent volume fractions remained the same between the two panels. All erosion test samples were machined into 25.4-mm-diameter disks.

Erosion Facility and Testing

A high-velocity (Mach 0.3 to 1.0) burner rig with erosion capability was used to create laboratory simulated turbine engine relevant erosion conditions. The development of the erosion rig along with computational fluid dynamics (CFD) modeling and experimental validation have been described in detail elsewhere (Refs. 5 to 8), but an overview of the facility is described here briefly.

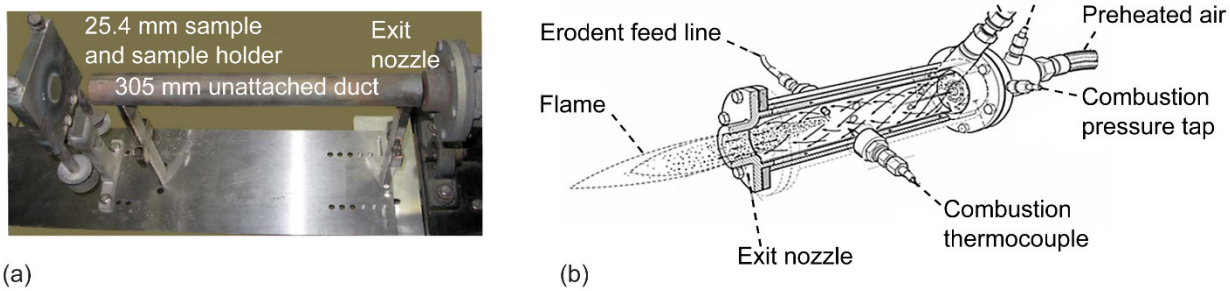

Figure 1.—Burner configuration. (a) Burner exit nozzle, unattached duct, and sample holder (Ref. 6). (b) Burner placed before duct (Ref. 8).

The erosion test facility is a modified NASA Glenn Mach 0.3 burner rig (Ref. 8) that operates on Jet-A fuel and preheated air. Erodent is delivered using a screw-driven powder feeder (HA 5000F-SA, Hardface Alloys, Inc.) where it is injected into the burner chamber, passes through a 19-mm exit nozzle, and accelerates downstream through a 19-mm-diameter, 305-mm-long unattached duct to the sample (Refs. 6 and 7). Uniform radial distribution of the erosion particles is achieved with the placement of the unattached duct after the burner nozzle creating a uniform erosion scar as predicted by CFD modeling and verified experimentally (Ref. 7). A high-temperature, spring-loaded, clamshell fixture, fabricated from Inconel® 601, is used to hold the sample during testing. A photograph of the burner exit nozzle, the unattached duct, and sample holder is displayed in Figure 1(a), and a schematic of the burner placed just before the duct is shown in Figure 1(b). The standoff distance between the duct exit and the center of the sample was set to 30 mm.

Samples were heated to 1,200 °C, as measured by a Williamson Corporation two-color pyrometer, where they were then exposed to 150-μm mean particle diameter alumina (Al_2O_3) particles. The particles were fed into the burner at a rate of 2 g/min. Three different particle velocities; 100, 150, and 200 m/s were used. The angle of particle impingement was varied between 30° and 90° for the 100-m/s particle velocity case to understand the effect of impingement angle on the erosion rate.

Particle velocities were measured using double disk velocimetry, as commonly used in erosion experiments (Refs. 9 to 11), but adapted for use at elevated temperatures by fabricating the disks using Inconel® 601. A schematic of the double disk is shown in Figure 2. In this method, two disks rotate on a common axis parallel to the erosive particle stream. The first disk (Disk 1), closet to the exit of the duct, contains a slit that allows the particles to pass through and impinge on the second disk (Disk 2). For a fixed angular velocity, ω, and a fixed separation distance, L, between the two disks, the erosion scar on Disk 2 relative to the slit on Disk 1, represented by the angle, θ, is related to the particle velocity, ν, based on the following relationship:

$$\nu = \frac{\omega L}{\theta} \tag{1}$$

The sensitivity of the method was improved by rotating the disks clockwise to obtain one erosion scar, and then rotating the disks counterclockwise to obtain a second erosion scar. This routine doubled the distance (2θ) between the scars to improve the accuracy of the measurements as performed by Wiederhorn and Hockey (Ref. 11).

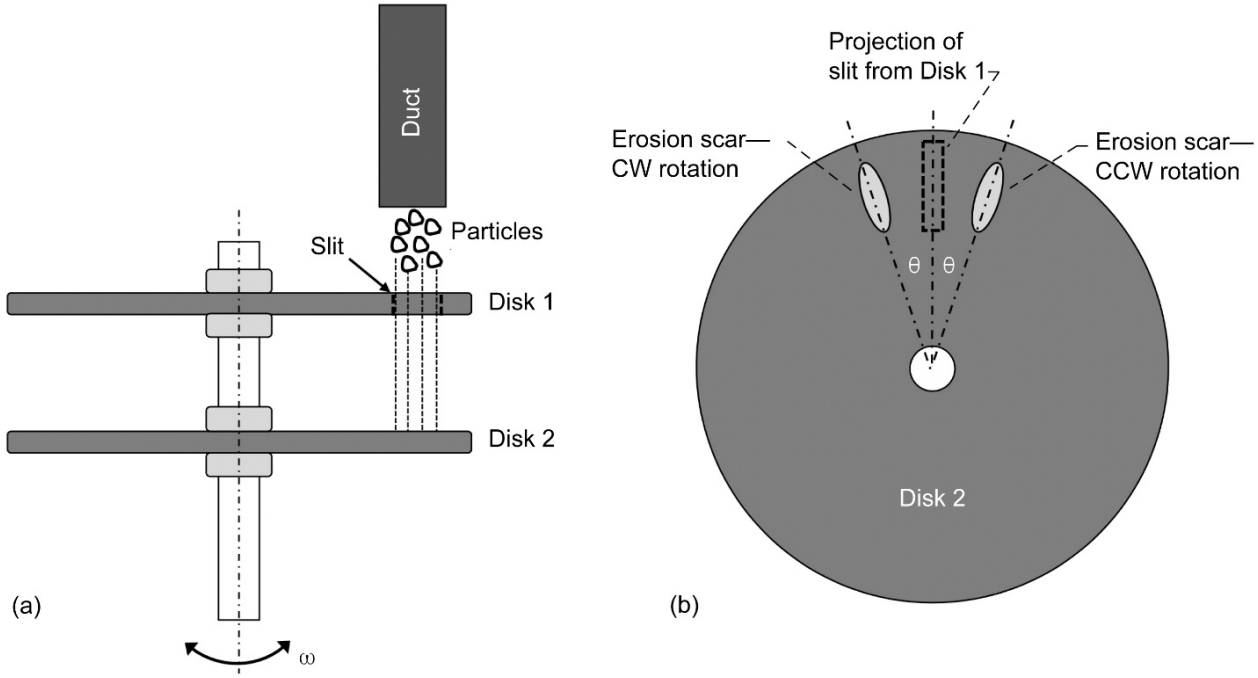

Figure 2.—Double disk velocimeter used to measure particle velocities. (a) Top-down view of apparatus. (b) Front view of Disk 2 after particle exposure. Clockwise (CW). Counterclockwise (CCW).

During erosion testing, samples were subject to multiple exposures where the sample mass was measured prior to erosion and after each successive exposure using a scale with precision of 0.01 mg. The steady-state erosion rates were then determined from a regression fit in the linear region of the cumulative mass loss versus cumulative mass erodent curve. For consistency, the regression analysis was performed on the last six data points of each curve. The erosion damage was characterized by SEM where the damage morphology was assessed directly from the eroded surfaces.

Results and Discussion

The dependence of the erosion rate on particle velocity and impingement angle are presented along with representative SEM images elucidating the governing erosion damage mechanisms.

Effect of Particle Velocity

Exemplary cumulative mass loss versus cumulative mass erodent curves are shown in Figure 3 for the MI SiC/SiC CMC at normal (90°) impingement for the three different velocities tested. First, a well-defined linear region (representing steady state) is observed after some initial nonlinear, transient region at each velocity. The initial transient region is generally represented by an initial sharp increase in mass loss (high slope) at low particle exposure, followed by a gradual decrease in slope until steady state is reached.

Furthermore, an increase in mass loss and steady-state erosion rate is observed as the particle velocity increases from 100 to 200 m/s where the increase in steady-state erosion rate as a function of particle velocity is shown in Figure 4. The erosion rate for the MI SiC/SiC CMC exhibits a power law relationship with respect to ν of the form:

$$E = \phi \nu^{n} \tag{2}$$

where $\phi = 1.7\times10^{-4}$ and $n = 2.2$.

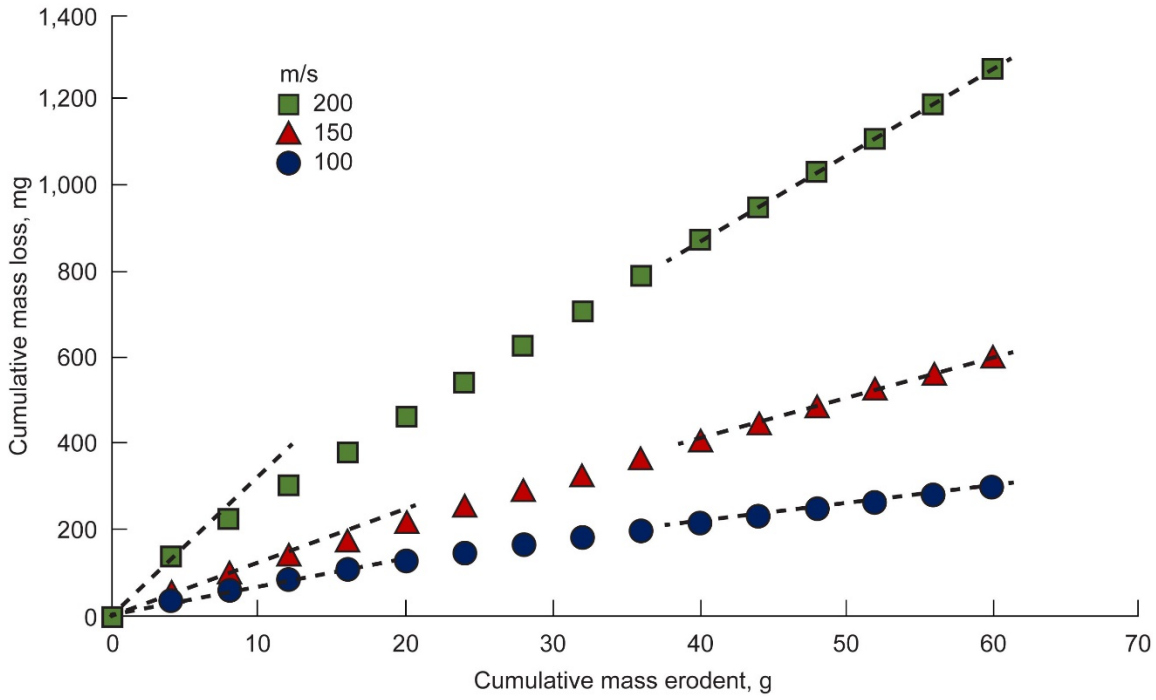

Figure 3.—Cumulative mass loss versus cumulative mass erodent curves for particle velocities v = 100, 150, and 200 m/s and 90° impingement.

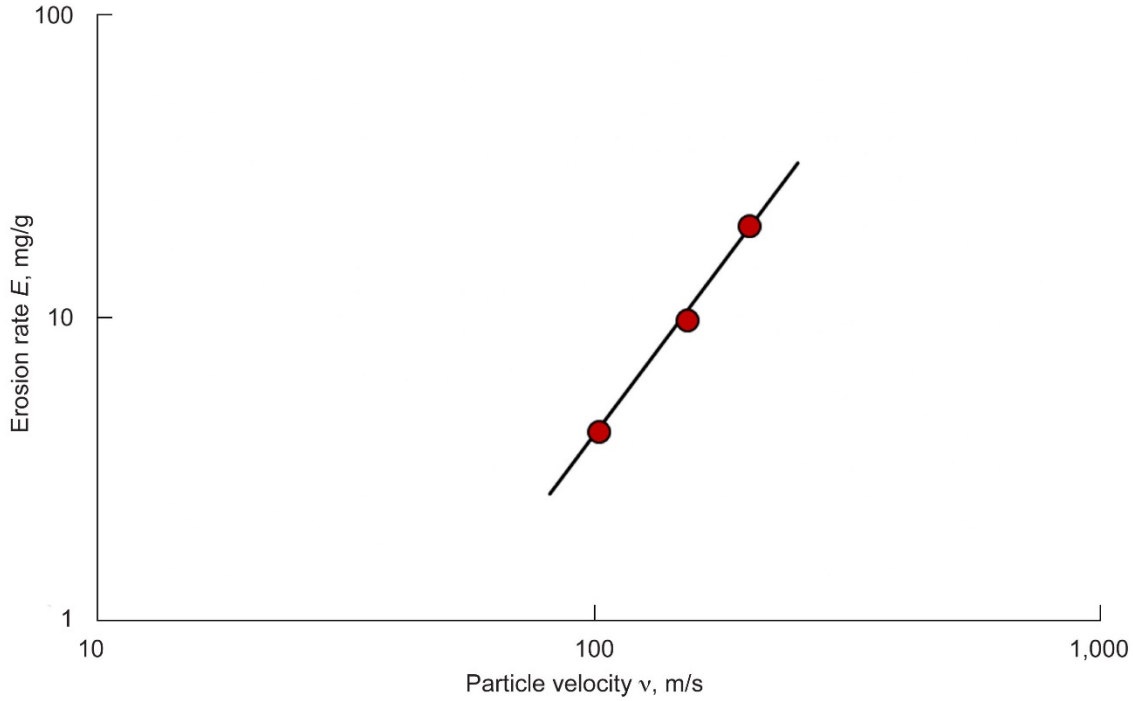

Figure 4.—Erosion rate as function of particle velocity at 90° impingement. $E = 1.7\times10^{-4}v^{2.2}$ (solid line).

Despite possessing a more complex microstructure (fibers, matrix, and interphase), the velocity dependence for the MI SiC/SiC CMC obtained in this study of $n = 2.2$ compares favorably to that predicted by the quasi-static indentation-induced fracture models for erosion of monolithic brittle solids where the dominant material removal mechanism is through the formation and propagation of subsurface lateral cracks.

The quasi-static indentation fracture model based on work by Wiederhorn and Lawn (Ref. 12) expresses the erosion rate, E in units of mass/mass as

$$E \propto \nu^{2.44} D^{0.67} \rho^{0.22} K^{-1.33} H^{0.11} \tag{3}$$

where D is the particle diameter, ρ is the particle density, K is the target fracture toughness, and H is the target hardness. Marshall, Lawn, and Evans (Ref. 13) presented a modified quasi-static erosion model expressed as

$$E \propto \nu^{2.33} E_m^{1.25} K^{-1} H^{-1.42} \tag{4}$$

where E_m is the elastic modulus of the target material. While some of the properties and exponents in both formulations differ, the predicted velocity dependence for lateral crack dominated material removal is similar, $n = 2.44$ (Eq. (3)) and $n = 2.33$ (Eq. (4)). As such, the comparable velocity exponent, $n = 2.2$ obtained experimentally for the MI SiC/SiC CMC suggests that lateral cracking may be an operative mechanism in the erosion behavior of the composite under these conditions.

Effect of Particle Impingement Angle

The effect of impingement angle on the erosion behavior in the MI SiC/SiC CMC was further evaluated. Typical cumulative mass loss versus cumulative mass erodent curves are shown in Figure 5. Similar to normal impingement, an initial high rate of mass loss is observed at low particle exposures for each impingement angle prior to reaching steady state. It is also evident that the total mass loss for a given particle exposure decreases as the impingement angle decreases. Assuming that the erosion process is controlled by brittle facture through the formation and propagation of lateral cracks, it has been suggested that the erosion response at oblique angles would be controlled by the normal component (indenting component) of ν, $\nu \sin \alpha$ where α is the impingement angle (Refs. 14 and 15). This would imply that

$$E \propto (\nu \sin \alpha)^n \tag{5}$$

Figure 6 shows a normalized steady-state erosion rate, E^* plotted as a function of α along with the $\sin^n \alpha$ law where $n = 2.2$ as experimentally determined from normal impingement. The E^* decreases as α decreases from a maximum at 90°, a characteristic of monolithic brittle solids. However, E^* becomes increasingly underpredicted by the $\sin^n \alpha$ law as α decreases. This suggests that there may be an increasing contribution of the tangential component of velocity, which may indicate a larger component of plastic deformation as α decreases. Evidence of increased plasticity at lower α have been reported in other ceramic materials particularly at elevated temperatures (Refs. 14 to 18).

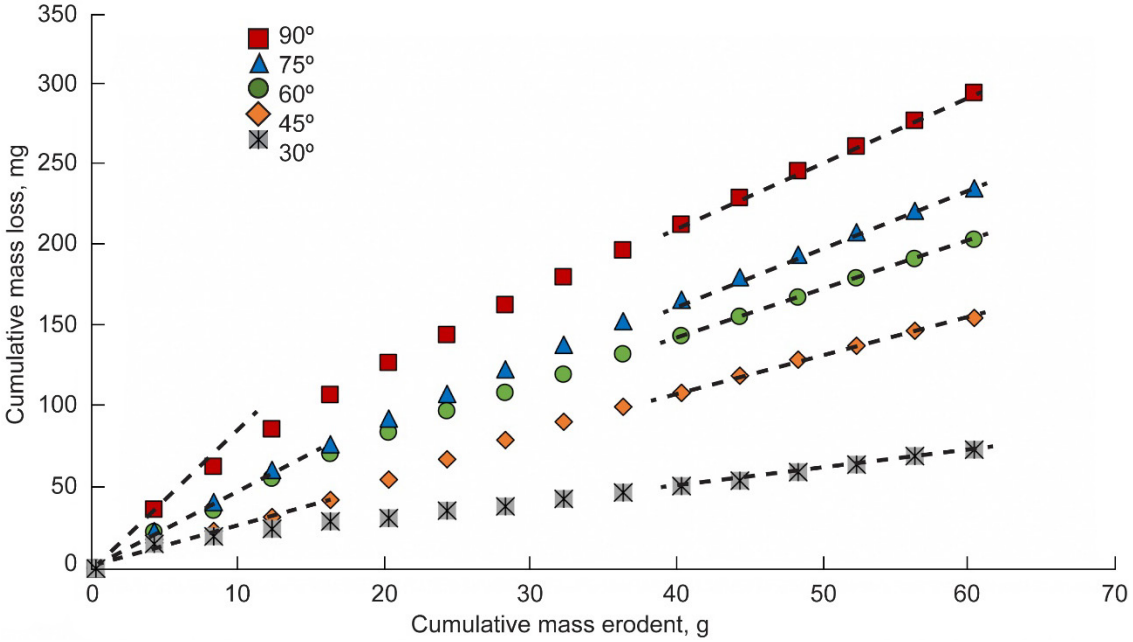

Figure 5.—Cumulative mass loss versus cumulative mass erodent for particle velocity, ν = 100 m/s at various particle impingement angles: 30°, 45°, 60°, 75°, 90°.

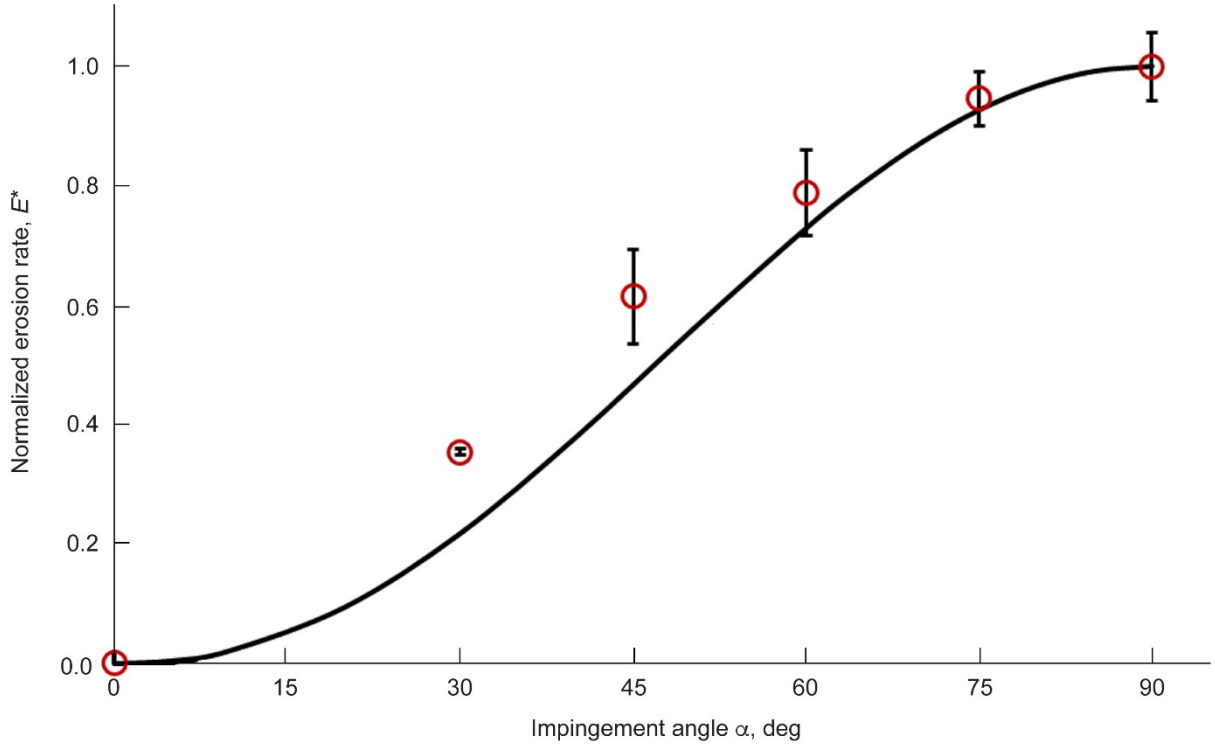

Figure 6.—Normalized steady-state erosion rate, *E**, plotted as function of particle impingement angle, α, at particle velocity, ν = 100 m/s. Also shown is $\sin^n \alpha$ law where *n* is the experimentally determined velocity exponent determined at 90° impingement; $\sin^{2.2} \alpha$ (solid line).

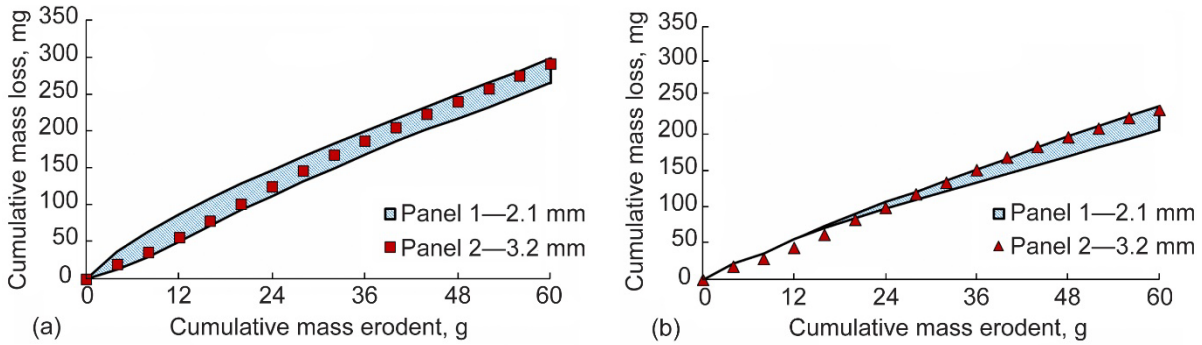

Figure 7.—Cumulative mass loss versus cumulative mass erodent from two composite panels at particle velocity, ν = 100 m/s. Shaded regions represent band of curves obtained from Panel 1 while solid symbols represent curves obtained from Panel 2. (a) 90° impingement. (b) 60° impingement.

Consistency in Erosion—Panel-to-Panel Variation

Samples tested under the same conditions, but from separate panels, were compared to understand the panel-to-panel consistency or variation in the erosion response. As discussed previously, the constituent volume fractions remained the same between the two panels; however, Panel 1 consisted of eight plies with an average thickness of 2.1 mm while Panel 2 consisted of 12 plies with an average thickness of 3.2 mm. The difference in thickness between the panels and samples is expected to have a negligible effect on the erosion response considering both panels had similar volume fractions, and due to the localized nature of erosion damage where any significant subsurface damage through the thickness is absent (Refs. 2 to 4). This is in contrast to large particle impact, where significant subsurface damage through the thickness can occur, and where the particle kinetic energy is large enough to cause additional damage through flexure depending upon the support configuration (Refs. 19 and 20).

Figure 7 shows a comparison of the cumulative mass loss versus cumulative mass erodent curves between the two panels at ν = 100 m/s for 90° impingement, and at an oblique angle of 60°. The shaded regions in Figure 7(a) and (b) represent the band of curves obtained for Panel 1 while the curves represented by the solid symbols were obtained for Panel 2. The data generated from Panel 2 generally falls within the range of data obtained from Panel 1, which demonstrates consistency and negligible variation in the erosion response and properties between the two panels tested in this work.

Erosion Damage Morphology

To understand the operative erosion mechanisms, the damage was assessed directly from the eroded surfaces for steady state and isolated particle impact conditions.

Steady-State Erosion Surface Morphology

Figure 8 shows steady-state erosion surfaces of the MI SiC/SiC CMC for 90° and 30° impingement angles at a particle velocity, ν = 100 m/s. For 90° impingement, Figure 8(a) and (b) show resultant erosion surfaces in a matrix-rich region where it is indicative that the material removal primarily occurs by a brittle chipping mode. In a fiber-rich region, Figure 8(c), extensive fiber breakage is observed. The fibers appeared highly susceptible to breakage upon particle impact once the surrounding matrix material was removed. For the 30° impingement, Figure 8(d) and (e), the erosion surfaces are characterized more by small wear scars and grooves reminiscent of material removal through a ductile ploughing process.

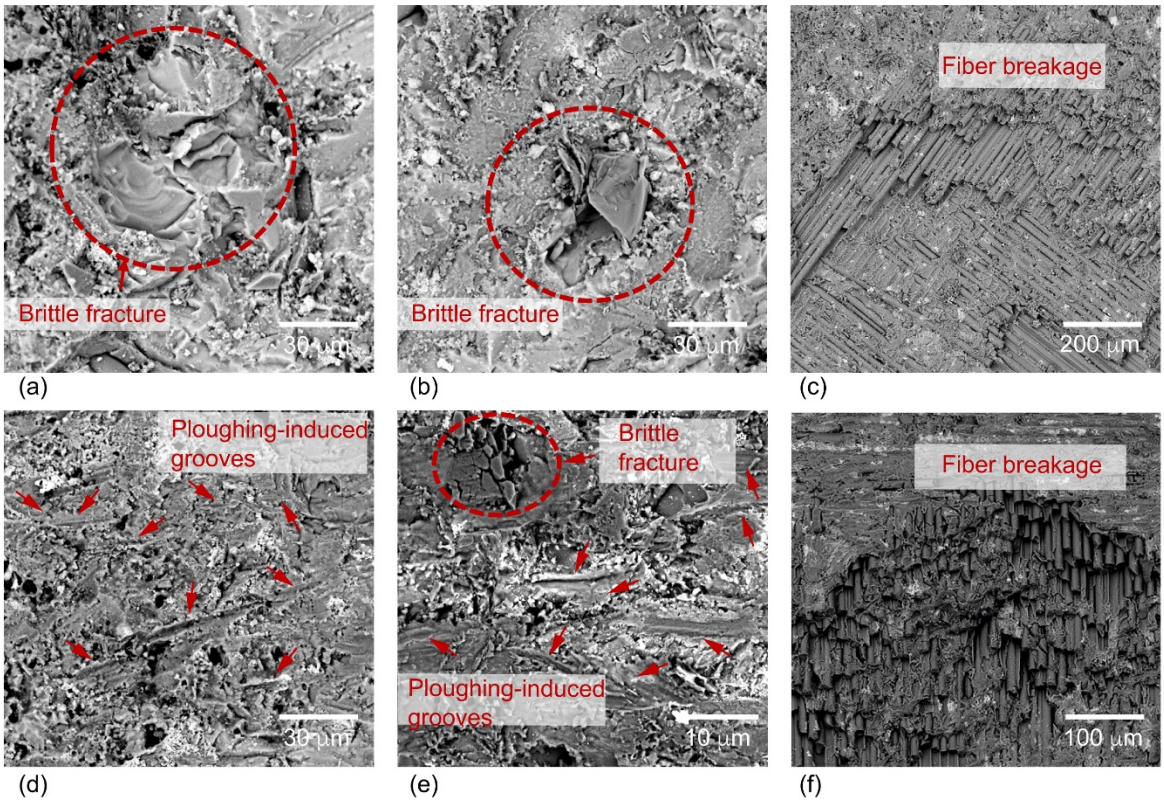

Figure 8.—Steady-state erosion surface morphologies for particle velocity, ν = 100 m/s. Particle impingement angle 90°. (a) Brittle fracture. (b) Brittle fracture. (c) Fiber breakage. Particle impingement angle 30°. (d) Ploughing-induced grooves. (e) Brittle fracture and ploughing-induced grooves. (f) Fiber breakage.

As shown in the area inscribed in the circle in Figure 8(e), evidence of brittle fracture by a chipping mode of erosion is still observed at the lower impingement angles. Moreover, extensive fiber damage at the lower impingement angles is still evident as displayed in Figure 8(f). Similar morphologies were also observed at the higher particle velocities (i.e., ν = 150 and 200 m/s).

Isolated Particle Impacts

To better understand the operative material removal mechanisms, some samples were subject to low levels of erodent (~0.1 g)[1] to investigate the onset of damage. Due to the small amount of exposure to erodent, isolated areas of damage were often discernable. Figure 9(a) shows an isolated impact event at 90° impingement and ν = 100 m/s in a matrix-rich region of the MI SiC/SiC CMC where lateral cracking and evidence of chipping resulting from the formation of the lateral crack is apparent. Figure 9(b) encompasses several impact events at 30° impingement and ν = 100 m/s in a matrix-rich region. Here, visible grooves produced by the ploughing action of the particles are observed.

Moreover, evidence of lateral cracking adjacent to the grooves imply that both lateral cracking (brittle mode) and ploughing (ductile mode) are operative at lower impingement angles, and act jointly to remove material. This supports the reasoning for the underprediction of the erosion rate by the $\sin^n \alpha$ law (Figure 6), which assumes that only the brittle (indentation) mode of erosion is operative through all impingement angles.

[1]Erodent was fed into the burner rig for ~3 s at the 2-g/min feed rate to achieve a dose of ~0.1 g.

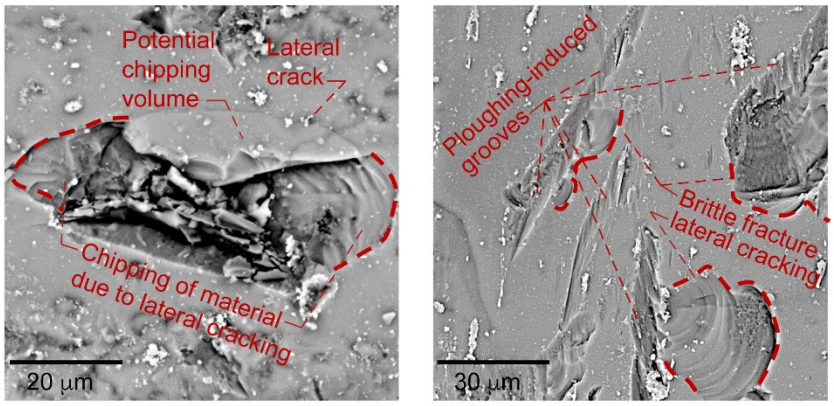

(a) (b)

Figure 9.—Isolated impact events in matrix-rich region at particle velocity, ν = 100 m/s. (a) 90° particle impingement. (b) 30° particle impingement.

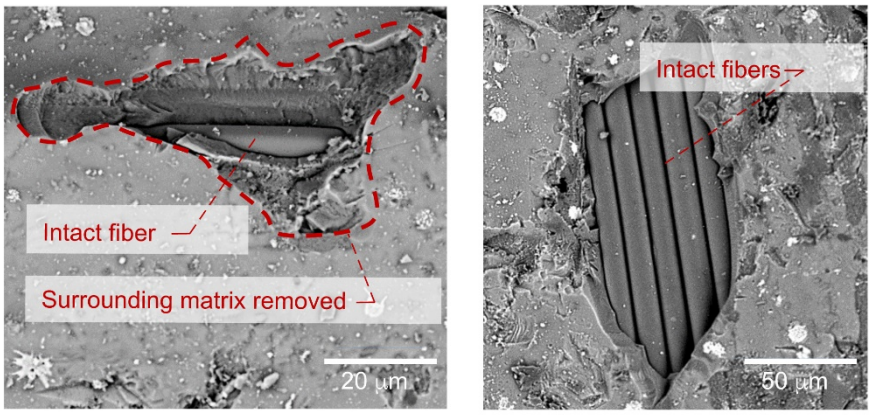

(a) (b)

Figure 10.—Regions of exposed fibers and fiber tows resulting from ejection of surrounding matrix material at 90° particle impingement and velocity, ν = 100 m/s. (a) Surrounding matrix removed showing a single intact fiber. (b) Surrounding matrix removed showing multiple intact fibers.

For isolated impacts in close proximity to fibers, it appears that the weak fiber and matrix interface, which is important for the enhanced damage tolerance and toughness observed in these composites, is preferential for crack propagation induced upon particle impact. Regions of exposed, but intact, fibers and fiber tows are observed as a result of ejected matrix material due to subsurface crack propagation occurring along the weak interface as shown in Figure 10. The exposed fibers are highly susceptible to impact damage and are readily fractured and removed upon successive particle impacts.

Conclusions

Solid particle erosion in ceramic matrix composites (CMCs) is a complex process and a function of many variables that will change under different operating conditions and environments. The CMC material properties, protective coating application (thermal and environmental barrier coatings), erosion conditions (particle composition, size, shape, velocity, impingement angle, etc.), and engine operational conditions (temperature, pressure, etc.) will all play a role in the overall erosion response of CMCs. As the use of CMC hardware in gas-turbine engines increase, it is critical to continue to develop an

understanding of the operative erosion mechanisms under different conditions. This is particularly important for cases of compromised thermal and environmental barrier coatings where the underlying CMC is being directly exposed to erosive particulates. Furthermore, developing a fundamental understanding of the erosion processes in CMCs can lead to improved design and fabrication of erosion-resistant CMCs, and to the formulation of appropriate physics-based erosion models.

Subject to the erosion conditions used in this work, the melt-infiltrated (MI) silicon carbide fiber-reinforced silicon carbide (SiC/SiC) CMC was shown to have an initial sharp increase in mass loss followed by a gradual decrease to steady state. The steady-state erosion rate at 90° impingement followed a power-law dependence with respect to particle velocity, v, where $E \propto v^n$, and $n = 2.2$. The velocity exponent, n, correlated well to that predicted by quasi-static erosion models based on indentation fracture and lateral cracking dominated material removal. The scanning electron microscopy (SEM) images revealed that lateral cracking is an operative mechanism responsible for material removal in the MI SiC/SiC CMC. Additionally, the weak fiber-matrix interface appeared to be preferential for crack propagation resulting in ejected matrix material exposing underlying fibers and fiber tows. Once exposed, the fibers were observed to be highly susceptible to particle impact and readily removed. As the particle impingement angle decreased from 90°, a plastic ploughing process played an increasing role in the erosion process where the brittle (indenting) mode and ductile (ploughing) mode acted jointly in the material removal process as evidenced by SEM of the eroded surfaces. Finally, erosion testing was performed on a separate panel to investigate any panel-to-panel variation in the erosion behavior. Negligible variation was observed between panels highlighting a consistency in the erosion response and properties of the MI SiC/SiC CMC investigated in this study.

References

1. Zok, F.W.: Ceramic-Matrix Composites Enable Revolutionary Gains in Turbine Engine Efficiency. Am. Ceram. Soc. Bull., vol. 95, no. 5, 2016, pp. 22–28.
2. Kedir, N., et al.: Erosion in Gas-Turbine Grade Ceramic Matrix Composites. J. Eng. Gas Turb. Power, vol. 141, no. 1, 2019, pp. 011019-1–011019-9.
3. Presby, M.J., et al.: Erosion in a Melt-Infiltrated SiC/SiC Ceramic Matrix Composite. J. Eng. Gas Turb. Power, vol. 142, no. 4, 2020, pp. 041009-1–041009-9.
4. Presby, M.J., et al.: Erosion Behavior in a Gas Turbine Grade Oxide/Oxide Ceramic Matrix Composite. Proceedings of the 42nd International Conference on Advanced Ceramics and Composites: Ceramic Engineering and Science Proceedings, vol. 39, no. 2, 2019, pp. 15–25.
5. Kuczmarski, Maria A.; Miller, Robert A.; and Zhu, Dongming: CFD-Guided Development of Test Rigs for Studying Erosion and Large-Particle Damage of Thermal Barrier Coatings. Modelling and Simulation in Engineering, Vol. 2011, Article ID 837921, Hindawi Publishing Corporation, London, England, 2011.
6. Miller, Robert A.; Kuczmarski, Maria A.; and Zhu, Dongming: Burner Rig With an Unattached Duct for Evaluating the Erosion Resistance of Thermal Barrier Coatings. NASA/TM—2011-217008, 2011. http://ntrs.nasa.gov
7. Miller, R.; and Kuczmarski, M.: Burner Rig for Small Particle Erosion Testing of Thermal Barrier Coatings. J. Test. Eval., vol. 42, no. 3, 2014, pp. 648–658.
8. Fox, Dennis S., et al.: Mach 0.3 Burner Rig Facility at the NASA Glenn Materials Research Laboratory. NASA/TM—2011-216986, 2011. http://ntrs.nasa.gov
9. Ruff, A.W.; and Ives, L.K.: Measurement of Solid Particle Velocity in Erosive Wear. Wear, vol. 35, 1975, pp. 195–199.

10. Stevenson, A.N.J.; and Hutchings, I.M.: Scaling Laws for Particle Velocity in the Gas-Blast Erosion Test. Wear, vols. 181–183, 1995, pp. 56–62.
11. Wiederhorn, S.M.; and Hockey, B.J.: Effect of Material Parameters on the Erosion Resistance of Brittle Materials. J. Mater. Sci., vol. 18, 1983, pp. 766–780.
12. Wiederhorn S.M.; and Lawn, B.R.: Strength Degradation of Glass Impacted With Sharp Particles: I, Annealed Surfaces. J. Am. Ceram. Soc., vol. 62, nos. 1–2, 1979, pp. 66–70.
13. Marshall, D.B.; Lawn, B.R.; and Evans, A.G.: Elastic/Plastic Indentation Damage in Ceramics: The Lateral Crack System. J. Am. Ceram. Soc., vol. 65, no. 11, 1982, pp. 561–566.
14. Srinivasan, Sreeram; and Scattergood, Ronald O.: R Curve Effects in Solid Particle Erosion of Ceramics. Wear, vol. 142, no. 1, 1991, pp. 115–133.
15. Hockey, B.J.; Wiederhorn, S.M.; and Johnson, H.: Erosion of Brittle Materials by Solid Particle Impact. Flaws and Testing. Fracture Mechanics of Ceramics, R.C. Bradt, D.P.H. Hasselman, and F.F. Lange, eds., Vol. 3, Springer, Boston, MA, 1978, pp. 379–402.
16. Zhou, Jianren; and Bahadur, Shyam: Erosion Characteristics of Alumina Ceramics at High Temperatures. Wear, vols. 181–183, pt. 1, 1995, pp. 178–188.
17. Routbort, J.L.; Scattergood, R.O.; and Turner, A.P.L.: Erosion of Reaction-Bonded SiC. Wear, vol. 59, no. 2, 1980, pp. 363–375.
18. Wellman, R.G.; and Allen, C.: The Effects of Angle of Impact and Material Properties on the Erosion Rates of Ceramics. Wear, vols. 186–187, 1995, pp. 117–122.
19. Bhatt, R.T., et al: Impact Resistance of Uncoated SiC/SiC Composites. Mater. Sci. Eng. A, vol. 476, nos. 1–2, 2008, pp. 20–28.
20. Choi, Sung: Foreign Object Damage Phenomenon by Steel Ball Projectiles in a SiC/SiC Ceramic Matrix Composite at Ambient and Elevated Temperatures. J. Am. Ceram. Soc., vol. 91, no. 9, 2008, pp. 2963–2968.